



Tracking intracellular forces and mechanical property changes in mouse one-cell embryo development

Marta Duch^{1,7}, Núria Torras^{1,6,7}, Maki Asami^{2,7}, Toru Suzuki^{2,7}, María Isabel Arjona^{1,3,7}, Rodrigo Gómez-Martínez¹, Matthew D. VerMilyea⁴, Robert Castilla⁵, José Antonio Plaza¹✉ and Anthony C. F. Perry²✉

Cells comprise mechanically active matter that governs their functionality, but intracellular mechanics are difficult to study directly and are poorly understood. However, injected nanodevices open up opportunities to analyse intracellular mechanobiology. Here, we identify a programme of forces and changes to the cytoplasmic mechanical properties required for mouse embryo development from fertilization to the first cell division. Injected, fully internalized nanodevices responded to sperm decondensation and recondensation, and subsequent device behaviour suggested a model for pronuclear convergence based on a gradient of effective cytoplasmic stiffness. The nanodevices reported reduced cytoplasmic mechanical activity during chromosome alignment and indicated that cytoplasmic stiffening occurred during embryo elongation, followed by rapid cytoplasmic softening during cytokinesis (cell division). Forces greater than those inside muscle cells were detected within embryos. These results suggest that intracellular forces are part of a concerted programme that is necessary for development at the origin of a new embryonic life.

Intracellular mechanics is a key determinant of cell biology. Each cell is mechanically stabilized by a filamentous cytoskeleton that controls relative stiffness¹. Active mechanical behaviour generates intracellular pulling and pushing forces and drives stochastic force fluctuation to enable cytoplasmic remodelling². Such dynamic mechanical intracellular behaviour provides a tier of regulation that may be as critical to developmental processes as regulation by gene expression^{3,4} and there is interplay between the two: force and stiffness changes control transcriptional programmes involved in cell differentiation^{5–7}.

Successful and comprehensive models of cell mechanics will require information on different hierarchical levels to relate local interactions in the cytoskeleton to the aggregate mechanical behaviour of cells^{1,8,9}. Broadly, there are two approaches to study cell mechanics: top-down (systems-level) and bottom-up (reductionist)^{1,10}. Top-down models are based on generic principles that are not obviously dependent on lower levels in the structure. These models are derived from extracellular devices^{1,9,11–14}. By contrast, bottom-up methods derive system properties from those of their constituents (for example, molecular assemblies including the cytoskeleton)^{1,8,9,11,15}.

Bottom-up approaches^{16–18} can be based on local intracellular measurements but the descriptions of constituent functions cannot necessarily be extrapolated to higher-order structures (for example, the cell) due to their complex heterogeneity¹. Thus, improved models of cell mechanical behaviour will be required that meet the considerable challenges of devising top-down direct intracellular models. Tools to complete the internalized top-down picture were

not available until recent advances in silicon-based nanodevices that can be reproducibly manufactured, are versatile and have the potential to be placed completely inside cells^{19,20}.

In the context of embryogenesis, externally induced stiffness in mouse embryonic stem cells influences the expression of pluripotency factors such as Oct4 to drive differentiation^{21,22}. In addition, endogenous mechanical transitions play a critical role in preimplantation development of mouse embryos after several days²³, but almost nothing is known about whether similar processes are important for embryonic development immediately after fertilization.

We accordingly sought an intracellular top-down approach to study the cytoplasmic mechanics of mammalian one-cell embryos (to the first mitotic cell division), which are relatively large: ~170 pl compared to ~1 pl for other mammalian cells^{24,25}. Such a large cellular volume could affect chromatin remodelling, intracellular transport (including pronuclear convergence) and cell division²⁶. Although this would suggest that intracellular forces and changes to the mechanical properties of the cytoplasm play a crucial role, no mechanical model accounts for them. We now detail direct mechanical readouts obtained following nanodevice injection and integrate them with molecular and gross morphological analyses. Results directly show an active programme of forces and mechanical property changes that drive early embryo development.

Results

Mass production of intracellular force-detecting nanodevices. Measuring intracellular embryonic mechanics required the scalable,

¹Instituto de Microelectrónica de Barcelona, IMB-CNM (CSIC), Esfera UAB, Campus UAB, Cerdanyola, Barcelona, Spain. ²Laboratory of Mammalian Molecular Embryology, Department of Biology and Biochemistry, University of Bath, Bath, UK. ³Departamento de Electrónica y Tecnología de Computadores, Facultad de Ciencias, Universidad de Granada, Granada, Spain. ⁴Ovation Fertility, Austin, TX, USA. ⁵LABSON - Department of Fluid Mechanics, ESEIAAT-Universitat Politècnica de Catalunya, Terrassa, Spain. ⁶Present address: Biomimetic Systems for Cell Engineering, Institute for Bioengineering of Catalonia, The Barcelona Institute of Science and Technology, Barcelona, Spain. ⁷These authors contributed equally: Marta Duch, Núria Torras, Maki Asami, Toru Suzuki, María Isabel Arjona. ✉e-mail: joseantonio.plaza@imb-cnm.csic.es; perry135@aol.com

high-fidelity production of force-change-sensitive chips that can be entirely internalized within mouse metaphase II (mII) oocytes. Such devices needed to be large enough to average out random (local) molecular perturbations so that their intracellular behaviour would reflect force fluctuations and changes in cytoplasmic stiffness (Supplementary Fig. 1). For a top-down model, relatively large two-dimensional devices are required (22 μm , similar to the diameter of the pronucleus, pn). This precludes the use of spherical three-dimensional tools of similar diameter, including some types of bead or oil droplet²⁷, whose large volumes could perturb cytoplasmic dynamics. Device thickness also had to be on the nanometre scale, akin to cytoskeletal structures (Fig. 1a), giving them an extraordinarily small volume and a high mechanical sensitivity.

To achieve these device dimensions, we employed silicon chip technology that should be achievable by MEMS laboratories. This technology permits a high degree of control and reproducibility over geometrical dimensions (Supplementary Fig. 2), allowing us to mass-produce complex three-dimensional 'H-comb' polysilicon-based nanodevices comprising eight cantilever prongs, with a total width of 10.5 μm (Fig. 1b,c, Supplementary Fig. 3 and Methods). A large device width solved the uncertainty of the maximum displacement, δ , determined by angular orientation (Supplementary Figs. 4 and 5). We produced $>1.5 \times 10^7$ device copies per 100-mm-diameter silicon wafer (Fig. 1d).

The cell interior has reduced inertial forces²⁸, and as a first approximation we modelled nanodevice bending on the basis of two representative simulations: a pressure, P , applied to the device surface, or a force, F , applied at the centre of the device (Fig. 1e, Supplementary Fig. 6 and Methods). As the nanodevices are free-floating, exhibit limited stiffness and possess small dimensions, their mechanical sensitivity was calculated by dimensional models, which are not restricted to simple structures, boundary conditions or loads. These methods were based on accurate experimental determination of the dimensions (Supplementary Fig. 2 and Methods) and Young's modulus of the nanodevice polysilicon layer (Supplementary Figs. 7 and 8 and Methods). Simulations predicted extremely low stiffness, with sensitivity to minute load states of $K_p = 35 \text{ Pa } \mu\text{m}^{-1}$ and $K_f = 3.39 \text{ nN } \mu\text{m}^{-1}$ (Fig. 1f), and revealed that the initial curvature of the devices due to fabrication did not affect mechanical sensitivity (Supplementary Fig. 9 and Methods).

Nanodevice mechanical sensitivity in mouse one-cell embryos.

There are few, if any, reports of cells harbouring entirely internal exogenous artefacts of $>10 \mu\text{m}$ and it was unclear whether mII oocytes would survive injection or tolerate the presence of such large (if extremely thin) structures. We evaluated different H-comb device lengths (22 and 42 μm) and thicknesses (25–500 nm); all were 10.5 μm wide. Microinjection precisely delivered fully internalized nanodevices into the cytoplasm of mII oocytes by membrane puncture (Supplementary Fig. 10a,b). Nanodevice volumes were small compared to the volume of mII oocytes (with volume ratios of $\leq 3.4 \times 10^{-4}$); oocytes could survive injection with devices of all thicknesses (Supplementary Fig. 10a).

Coinjecting mII oocytes with $22.0 \times 10.5 \times 0.025 \mu\text{m}^3$ H-comb nanodevices and sperm heads permitted nanodevice delivery and fertilization in the same procedure so that force changes could be captured from the earliest moments of development in the resulting embryo (Supplementary Fig. 10c,d). One-cell embryos containing H-comb nanodevices expressed genes at control levels (Supplementary Fig. 10e), consistent with normal development. Oocytes coinjected with sperm plus nanodevices or multiple $3.0 \times 3.0 \times 0.025 \mu\text{m}^3$ control nanosquares produced embryos that developed at high rates ($90.0 \pm 10.0\%$) to form expanded blastocysts expressing the pluripotency marker, Oct4 in the control range (Supplementary Fig. 10f–j), indicative of healthy development and lineage specification after nanodevice injection.

We found no evidence of direct interaction between cytoskeleton and injected nanodevices or microspheres throughout the first embryonic cell cycle (Supplementary Fig. 11a,b), even though microtubules were readily shown to interact with control, DNA-labelled latex beads (Supplementary Fig. 11c). Because the nanodevices were injected, they were not internalized by microfilaments¹⁷.

We investigated nanodevice behaviour in five nominal embryo phases: sperm decondensation, recondensation and pronucleus formation (SDR, corresponding to meiotic exit), pronuclear migration (PM, corresponding to G1 and S phases), pronuclear envelope breakdown (PEB) and chromosome mingling, embryo elongation (EL) just before division (presumptively initiating in G2 phase) and the first (one- to two-cell) mitotic division (DIV) (Fig. 1g,h). Nanodevices register intracellular mechanics of relatively large regions of cytoplasm (unlike small-scale measurements of individual random perturbations²): displacement, rotation and translation, contained information about the cytoplasmic reorganization and nanodevice deformation revealed force magnitudes (Fig. 2a–e, Supplementary Figs. 12 and 13 and Supplementary Video 1). To process this information, we propose two ad hoc theoretical parameters (Fig. 2f): $\xi_k = F_{\text{max}}/\text{Rot}_{\text{max}}$, related to resistance to cytoplasmic reorganization (F_{max} and Rot_{max} were, respectively, maximum force and rotation detected by the nanodevice), and $\xi_{\text{mact}} = (\Delta\delta_{\text{av}} \times \text{Rot}_{\text{av}})/\text{time}$, related to transitions in time-averaged mechanical activity (where time was the phase duration and $\Delta\delta_{\text{av}}$ and Rot_{av} are respectively averages of measured nanodevice bending and rotation during that time) (Fig. 2g). These parameters revealed that early mouse embryos exhibited programmed transitions in intracellular ξ_k and a range of several orders of magnitude in ξ_{mact} (Fig. 2f).

Major mechanical activity during paternal genome reprogramming.

Within 20 min of injection into mII oocytes, sperm heads started decondensing and increased roughly sevenfold in length (Fig. 2h–j and Supplementary Fig. 14) before recondensing and forming a visible pronuclear envelope^{29,30}, corresponding to the SDR phase, lasting 168 ± 27 min. Nanodevices were typically near the sperm head ($9.5 \pm 4.5 \mu\text{m}$; Fig. 2h) and rotated up to $44 \pm 1^\circ$, with elastic deformations of $1.5 \pm 0.8 \mu\text{m}$ (Fig. 2c,d,i). Maximal nanodevice deformation corresponded to $P = 56.2 \pm 28.7 \text{ Pa}$ ($1 \text{ Pa} = 1 \text{ pN } \mu\text{m}^{-2}$) and $F = 5.3 \pm 2.7 \text{ nN}$ (Fig. 2e). These results reveal major ξ_{mact} and thus cytoplasmic reorganization near the paternal genome during chromatin remodelling (Fig. 2f, j). Although direct force comparisons between studies are difficult, forces near to the sperm head were ~ 50 times larger than those inside aortic muscle cells measured with silicon nanowires (with peaks of 116 pN)¹⁷ and three orders of magnitude greater than forces exerted by single cytoskeletal motors ($<10 \text{ pN}$)³¹.

A cytoplasmic GES in embryos. Pronuclei appeared 4.0–4.5 h after fertilization and during PM converged on the embryo centre until membrane breakdown (Fig. 1g,h and Supplementary Fig. 15a), 812 ± 195 min after sperm injection (Fig. 2g)^{30,32}. On small spatiotemporal scales, PM was directionally stochastic (Fig. 3a) and accompanied by random ruffling of up to 2 μm at the embryo surface (Fig. 3b, Supplementary Fig. 15b and Supplementary Video 2); nanodevices also exhibited $\sim 2 \mu\text{m}$ random displacements even when close to the centre (Fig. 3c). Pronuclear and nanodevice random displacements reflected random kinetic activity and were concurrent with centralizing directional displacements (Fig. 3a,d). Nanodevices deformed by $1.3 \pm 0.1 \mu\text{m}$ (Fig. 2d), corresponding to loads of $47.9 \pm 6.1 \text{ Pa}$ and $4.5 \pm 0.5 \text{ nN}$ (Fig. 2e) and rotated $47.0 \pm 6.7^\circ$ (Fig. 2c), evidencing a programme of gradual (over several h) long-range cytoplasmic reorganization required for pronuclear convergence at the centre.

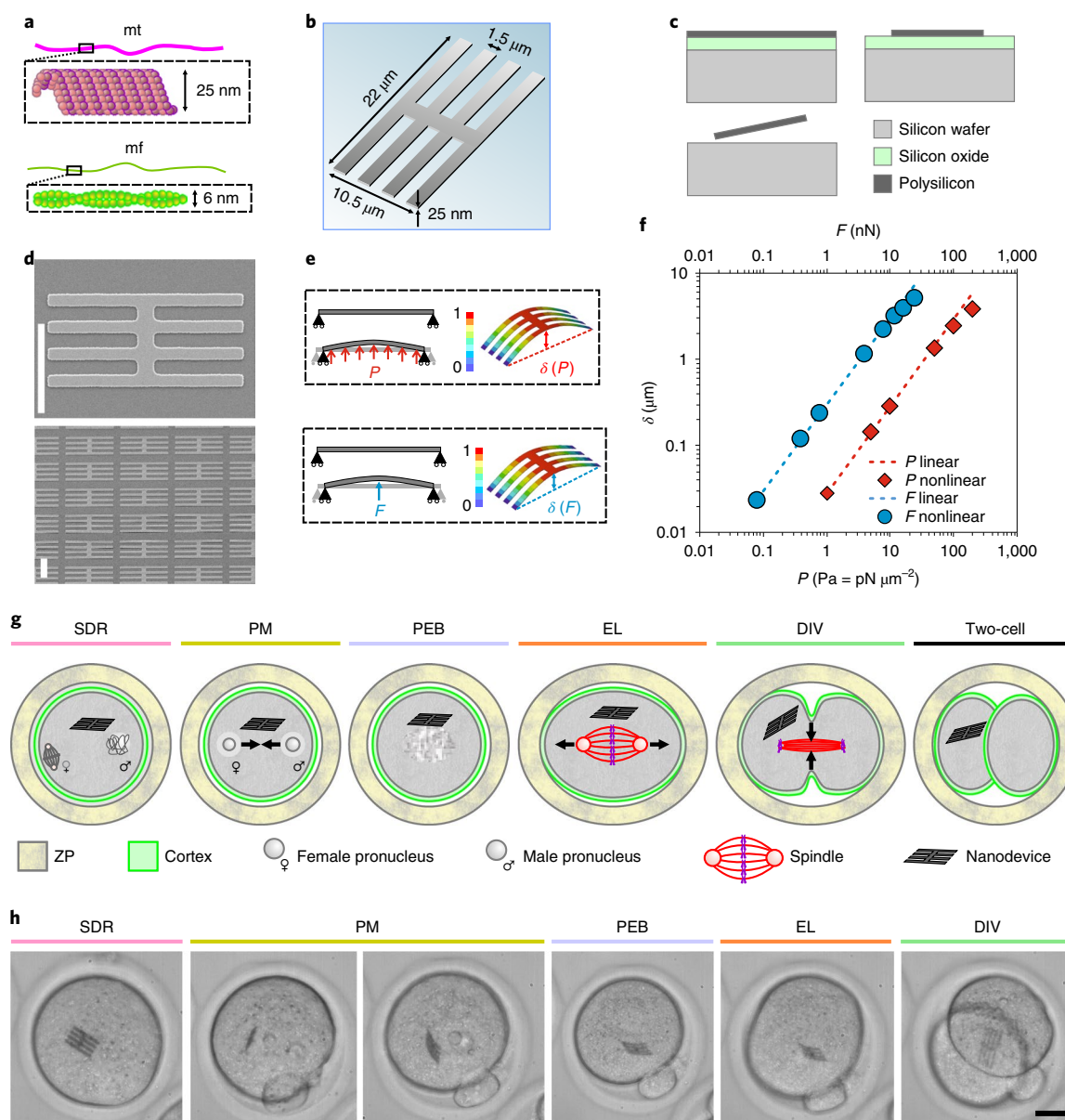


Fig. 1 | Fabricated nanodevices as intracellular sensors. **a**, Schematic of microtubules (mt) and actin microfilaments (mf). **b**, Geometry of fabricated 'H-comb' nanodevices. **c**, Schematic representation of nanodevice fabrication technology. Silicon oxide served as a sacrificial layer onto which was deposited a polysilicon structural layer. Photolithography combined with polysilicon etching delineated the device shape, followed by etching to remove the sacrificial layer. **d**, Scanning electron microscope image of a single nanodevice (top) and reproducible nanodevice batch fabrication. Scale bars, 10 μm . **e**, Device load state and simulated normalized vertical displacement by the finite element method for uniform distributed pressure load (P , top) and force loads (F). **f**, Simulated maximum vertical displacement versus applied pressure and force. **g**, Schematic representation of different stages in the mouse one-cell embryo (zygote) following fertilization, showing key structures in embryo mechanics and embryo stages. **h**, Vidcaps of mouse embryos at different stages, each containing a microinjected nanodevice. Scale bar, 20 μm .

Pronuclear centring has previously been attributed to an intracellular pressure gradient, predicting higher migration speeds for larger objects³³. To probe this model, we generated embryos containing microspheres that resembled pronuclei in shape and density (polyethylene microspheres of $1.00 \pm 0.01 \text{ g ml}^{-1}$)³⁴ but with a range of diameters (9.9–18.8 μm). Microspheres were injected with sperm, or without sperm followed by activation to produce haploid parthenogenotes. Most pronuclei were larger than the microspheres, with average diameters of $13.1 \pm 1.7 \mu\text{m}$ (maternal) and $19.8 \pm 0.3 \mu\text{m}$ (paternal) or $18.1 \pm 2.4 \mu\text{m}$ in parthenogenotes. In contrast to pronuclei and nanodevices within embryos, microspheres exhibited trajectories that tended to avoid the centre (Fig. 3d and Supplementary

Video 3), with no discernable correlation between microsphere maximum velocity and size (Fig. 3e). These observations and the finding that nanodevices near the centre underwent similar random displacements to those at the cortex (Fig. 3c), argued against the involvement of an intracellular pressure gradient alone³³.

The mechanical properties of mouse one-cell embryo cytoplasm can be modelled in terms of elastic and viscous elements using a combination of springs and dashpots³⁵. However, the influence of conditions at the embryo periphery (a stiff cortical system) on interior effective cytoplasmic mechanical properties, and their consequences for the movement of large organelles, have not been elucidated. The cytoplasm exhibits background random fluctuating

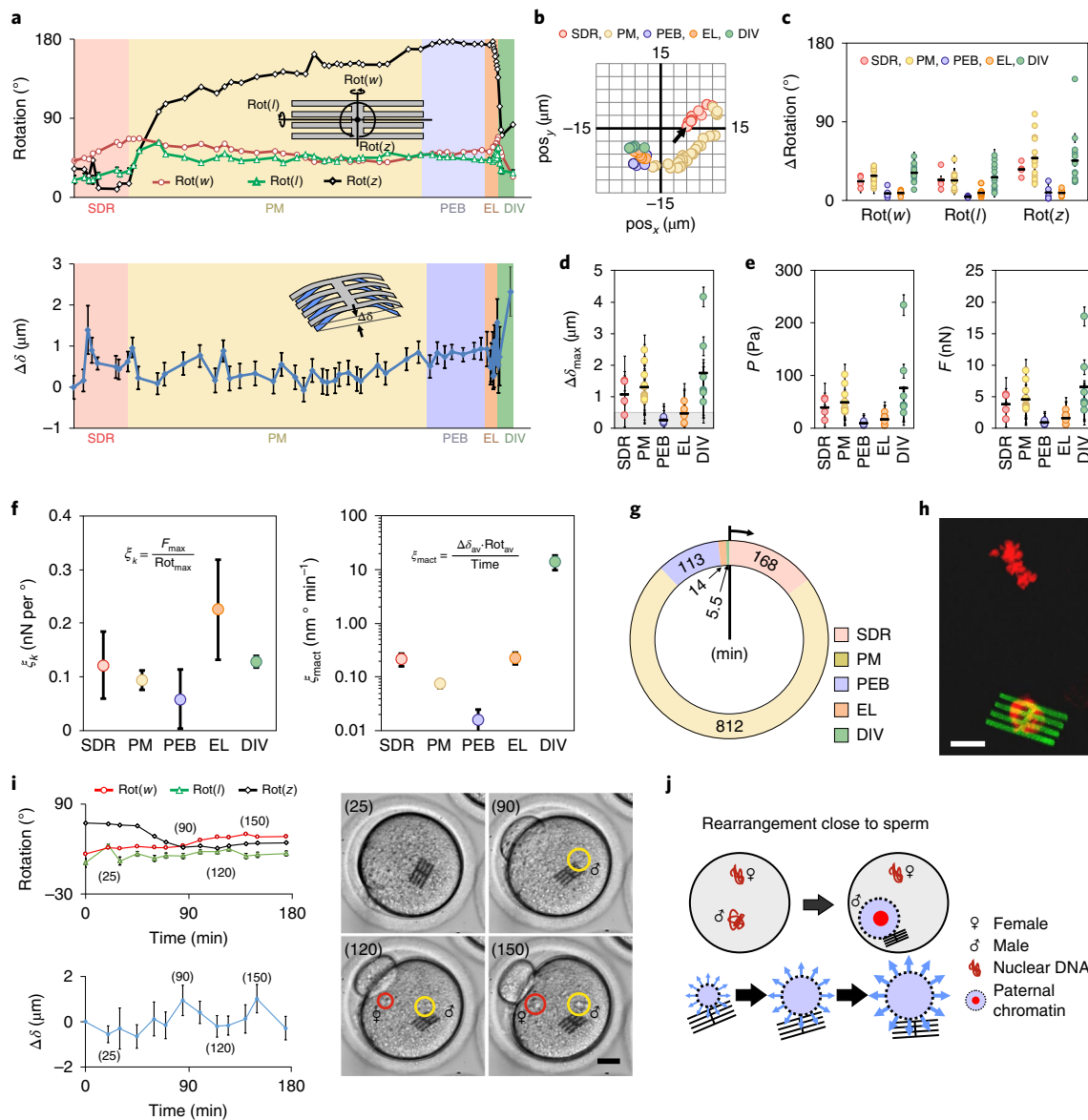


Fig. 2 | 'H-comb' nanodevices detect mechanical loads inside mouse zygotes. **a**, Representative plots showing rotations (Rot(w), Rot(l), Rot(z), top) and nanodevice deformation ($\Delta\delta$, bottom). Each background colour corresponds to one of the different embryonic stages of Fig. 1g,h. **b**, As per **a**, showing the two-dimensional nanodevice trajectory during different embryo stages. pos_x , position in x; pos_y , position in y. **c,d**, Maximum rotations (Rot(w), Rot(l), Rot(z)) (**c**) and $\Delta\delta$ (**d**) for each stage, with the range of lower confidence indicated in grey. $n=41$ for (Rot(w)), $n=43$ for (Rot(l)), $n=46$ for (Rot(z)) and $n=36$ for $\Delta\delta$. **e**, Simulation of the pressure or force on the nanodevice necessary to obtain given values of $\Delta\delta_{max}$. Error bars depict measurement uncertainty. Black horizontal lines in **c-e** show mean values. **f**, Transitions of ξ_k and ξ_{mact} . **g**, Average duration of each nominal stage of one-cell embryo (zygote) development. **h**, Fluorescence image of autofluorescing nanodevice (green), showing labelled oocyte- (top) or sperm-derived (bottom) chromatin (red). Scale bar, 10 μm . **i**, Rotation (Rot(w), Rot(l), Rot(z), top left) and $\Delta\delta$ (lower left) and images (right) at (25, 90, 120 and 150 min, as indicated). Red and yellow circles, respectively, indicate the positions of female and male chromatin. Scale bar, 20 μm . **j**, Schematic showing the displacement of the devices associated with paternal (sperm-derived) genome remodelling. Error bars in **a**, **c-f** and **i** depict error propagation. n refers to independent biological samples throughout.

forces that cover elastic and viscous regimes^{2,35}. Consistent with this, we found that elastic and viscous simulations (Fig. 3f) supported a model in which the embryo cytoplasm exhibits a gradient of effective stiffness (GES). In the GES model, the effective elastic constant and viscosity are increased by the relatively stiff cortical system in a manner that is also a function of the internal particle size. In agreement with this, the random migration of endogenous cytoplasmic particles is typically smaller the closer the particles are to the cortex (Supplementary Fig. 16 and Supplementary Video 4).

Although limited by inherent intraembryonic heterogeneity, the GES model predicts that an increase in pronuclear size during the PM

phase would favour movement towards the embryo centre, where the effective stiffness is smaller (Fig. 3g). This prediction was validated by real-time videomicroscopy revealing pronuclear expansion in mouse and human embryos (Fig. 3h and Supplementary Fig. 16).

In addition, assuming that the elastic contribution is greater in the direction of displacement, the GES model predicts that for any given position inside the embryo, the elastic constant for centralization is smaller than that for displacement to the periphery (Fig. 3i,j and Supplementary Fig. 15c-i). The primary consequence of this is that random forces induce centring of relatively large intracellular objects. To test this, we coinjected sperm and microspheres,

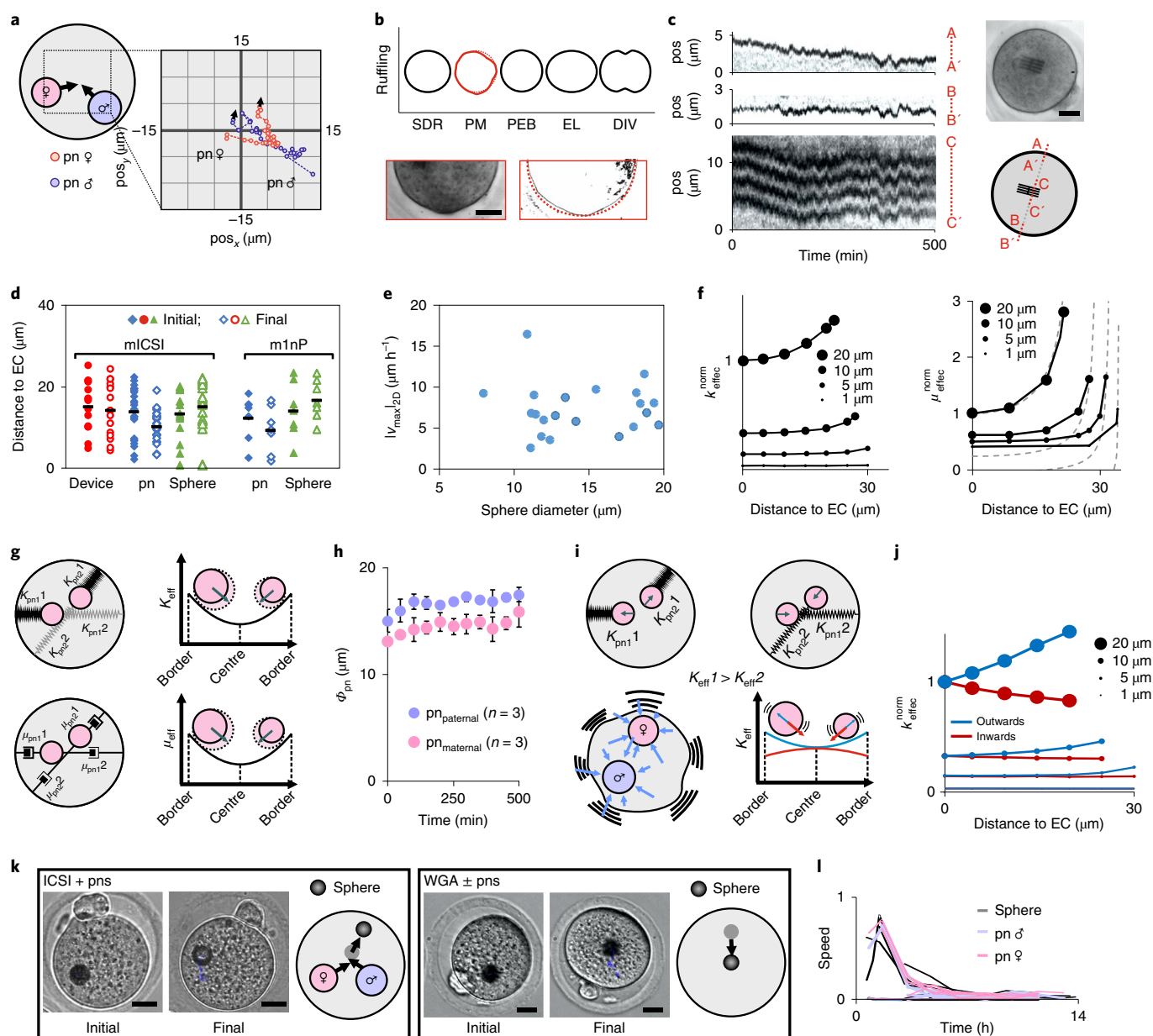


Fig. 3 | Mechanics during the PM phase. **a**, Two-dimensional pronuclear translations around the embryo centre. pos_x , position in x ; pos_y , position in y . **b**, Membrane ruffling showing (upper) schematic of external embryo morphology for different assigned phases, and (lower) images of half of an embryo during the PM phase (left), schematically rendered. **c**, Membrane topography changes at two opposite points and movement of the nanodevice (near the centre) with time. pos , scan position along AA', BB' and CC' versus time. **d**, Initial and final distances from the nanodevice ($n=15$), pronuclei ($n=26$) and microinjected microspheres ($n=21$) respectively to the embryo centre (EC) following sperm injection, showing corresponding values in haploid parthenogenetic embryos for pronuclei ($n=7$) and microspheres ($n=7$). Black horizontal lines show mean values. **e**, 2D maximum reported speed ($|v_{max,2D}|$) versus sphere diameters. **f**, Qualitative simulated normalized effective elastic constant (k_{eff}^{norm} , left) and viscosity (μ_{eff}^{norm} , right) for the displacement of spherical objects of different diameters versus the object position relative to the embryo centre. Dotted lines show theoretical values (valid for objects near the border). **g**, Schematic representations of the effective stiffness model for sphere centring with increasing size. **h**, Pronuclear expansion (ϕ_{pn} , mean \pm s.e.m.) determined by videomicroscopy analysis ($n=3$). **i**, Schematic showing the difference of effective stiffness outwards or inwards for pronuclei (top), embryo ruffling (bottom, left) and the corresponding effective stiffness. **j**, Qualitative, normalized effective elastic constants for the displacement of spherical objects of different diameters versus the relative position of the object to the embryo centre for **i**. **k**, Representative micrographs of oocytes injected with spheres plus sperm with (left) or without inhibiting ensuing pronucleus membrane formation using wheat germ agglutinin (WGA) ($n=2$ biologically independent experiments). The displacement tendency of microspheres is represented schematically in each case. **l**, Relative speeds of male pronuclei, female pronuclei and microspheres with time (0 shows a fertilization of +4 h). Scale bars, 20 μ m. n refers to independent biological samples unless stated otherwise.

but inhibited pronuclear formation with wheat germ agglutinin³⁶. In the absence of larger objects such as pronuclei, the GES model predicts that microspheres migrate to the embryo centre by random

displacements, which they did (Fig. 3k). Furthermore, in the absence of pronuclei, relatively large endogenous particles tend to locate away from the periphery (Supplementary Fig. 16).

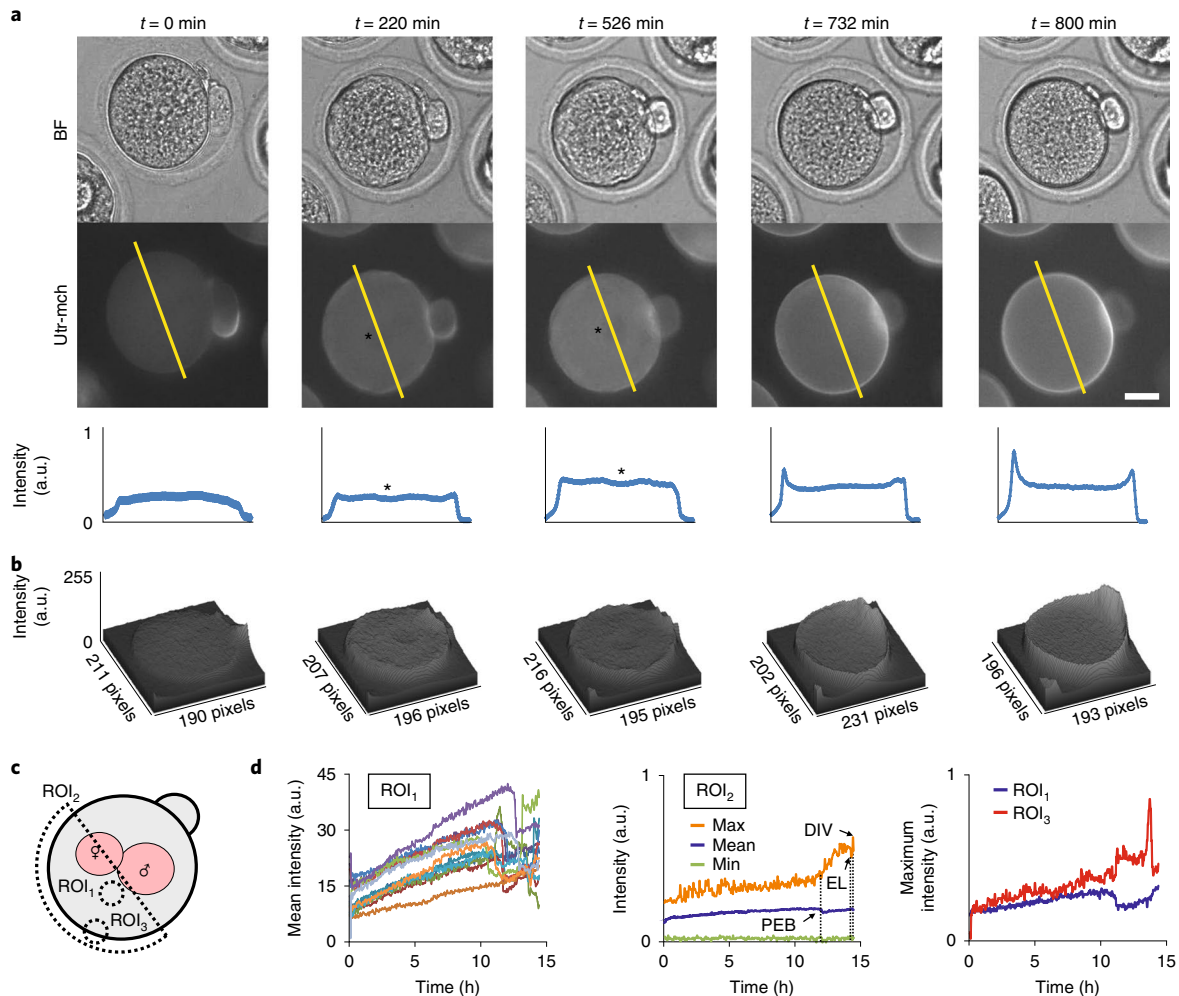


Fig. 4 | Dynamic F-actin redistribution in mouse zygotes. **a**, Representative ($n = 4$) vertically paired brightfield (BF, upper) and Utr-mCherry fluorescence (centre) vidcaps and profile line-plots from live embryos at the times indicated after pronucleus formation. Asterisks indicate pronuclear localization. Scale bar, $20\ \mu\text{m}$. a.u., arbitrary units. **b**, Three-dimensional surface plots of Utr-mCherry pixel intensity across a representative embryo of **a**. **c**, Schematic of the region of interest (ROI) for **d**. **d**, Utr-mCherry mean fluorescence intensity of representative embryos for region of interest, ROI₁ (left) (cytoplasm excluding pronuclei; $n = 11$), Utr-mCherry mean, minimum and maximum intensities for a representative embryo in ROI₂ (centre) (half of the embryo excluding polar bodies) and (right) maximum intensity of ROI₁ (cytoplasm) and ROI₃ (cortex). n refers to independent biological samples throughout.

The GES model also accounted for the slowing of pronuclei approaching the embryo centre, where the effective elastic constant (K_{effec}) and viscosity (μ_{effec}) difference in any direction are small (Fig. 3f,j). In addition, GES explains the increment of mechanical loads detected by nanodevices during this phase (Fig. 2e); this could also contribute to pronuclear centring.

Given that beads in the presence of typically larger pronuclei are excluded from the centre (Fig. 3d) and travel with speed profiles that overlap those of pronuclei (Fig. 3l), it is possible that large objects such as pronuclei dictate cytoplasmic rearrangements on large intracellular scales. This effect could be augmented by the previously reported^{33,37,38} existence of an F-actin cloud surrounding pronuclei and extending their effective diameter, which we corroborated by imaging the F-actin-binding protein, Utrophin (Utr) fused to mCherry (Utr-mCherry; Fig. 4a,b and Supplementary Videos 5 and 6).

Low cytoplasmic mechanical activity during spindle formation.

The PEB phase (lasting $113.0 \pm 30.8\ \text{min}$) (Fig. 2g) included spindle formation and chromosome alignment before the onset of EL. During the PEB phase, nanodevices reported cytoplasmic

mechanical load changes at the lower threshold of detection and the smallest of the entire embryo one-cell stage ($8.6 \pm 1.7\ \text{Pa}$, $0.8 \pm 0.2\ \text{nN}$) (Fig. 2e). Embryo surface membrane ruffling stopped simultaneously and abruptly with PEB (Supplementary Videos 5 and 6), in agreement with the minimal ξ_{mact} reported by the nanodevices (Fig. 2f). This coincided with a marked increment of cortical F-actin, reflecting actin redistribution from the embryo interior to cortex (Fig. 4a–d). A reduction of cytoplasmic forces during the PEB phase could facilitate spindle assembly and chromosome alignment.

Cytoplasmic stiffening governs EL. The EL phase lasted $14 \pm 2\ \text{min}$ and was characterized by spindle separation and embryonic axial elongation of $\sim 10\%$ ($\sim 8\ \mu\text{m}$) (Fig. 5a and Supplementary Video 7). After the embryo poles contacted the zona pellucida, EL continued at the same rate, $\sim 1.25\ \mu\text{m}\ \text{min}^{-1}$ (Fig. 5a). Motors driving spindle elongation thus generate forces that are sufficient to maintain overall cellular elongation at a constant rate with or without resistance from the zona pellucida. Signature plots for rates of axial elongation and equatorial contraction were conserved in mouse haploid parthenogenotes and most of the human embryos produced by

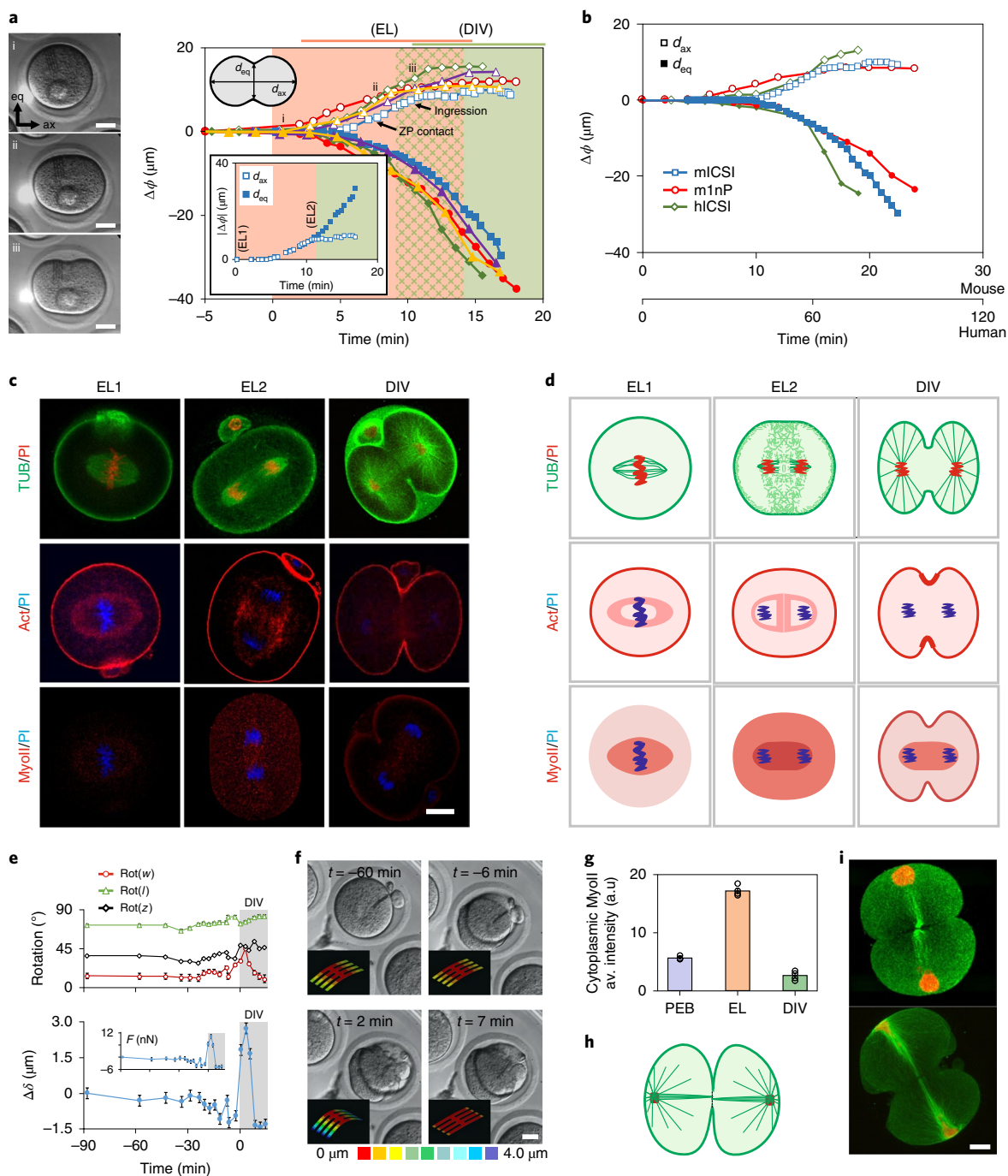


Fig. 5 | Morphological and cytoskeletal changes during elongation and division. **a**, Representative images (left, $n=8$) of EL, showing an initial stage before the onset of elongation (i), elongation in which zero axial cortical curvature is achieved in the equatorial region (ii) and EL after cleavage plane instatement (iii). Increment, $\Delta\phi$, of axial (d_{ax}) and equatorial (d_{eq}) diameters of five mouse embryos (right), showing absolute values of d_{ax} and d_{eq} diameter increments, $\Delta\phi$ (inset). Scale bar, 20 μm . **b**, Increment, $\Delta\phi$, of d_{ax} and d_{eq} are compared between mouse embryos generated by ICSI (mICSI; $n=8$), parthenogenotes (1nP; $n=4$ produced over $n=2$ independent experiments) and human embryos generated by ICSI (hICSI; $n=17$ obtained over $n=3$ independent experiments). **c**, Immunofluorescence images (top) of α -tubulin (TUB) showing microtubules in mouse one-cell embryos during initial spindle elongation (EL1), equatorial tubulin meshwork appearance (EL2) and after the appearance of radial microtubules and invagination (DIV). Immunofluorescence images (centre) of F-actin (Act) and myosin II (MyoII, bottom) showing a clear increase of myosin II after EL1 and a decrease after EL2. Genomic DNA is stained with propidium iodide (PI) in all the images. Scale bar, 20 μm . **d**, Corresponding schematic interpretations for **c**. **e**, Plots showing rotation (with corresponding forces) of intracellular nanodevices before and during the DIV phase, showing error propagation. **f**, Images of a representative embryo with corresponding simulated device deflections (insets). Scale bar, 20 μm . **g**, Average cytoplasmic myosin II intensity (determined by quantitative immunofluorescence \pm s.e.m.) at PEB, EL and DIV stages ($n=4$ each), showing an increase during the EL phase and a posterior decrease during the DIV phase. **h**, Schematic representation of microtubule distribution. **i**, Representative immunofluorescence micrographs ($n=2$) of α -tubulin showing microtubule (green) and nuclear DNA (red) distributions near the end of the DIV phase. Scale bar, 10 μm . n refers to independent biological samples unless stated otherwise.

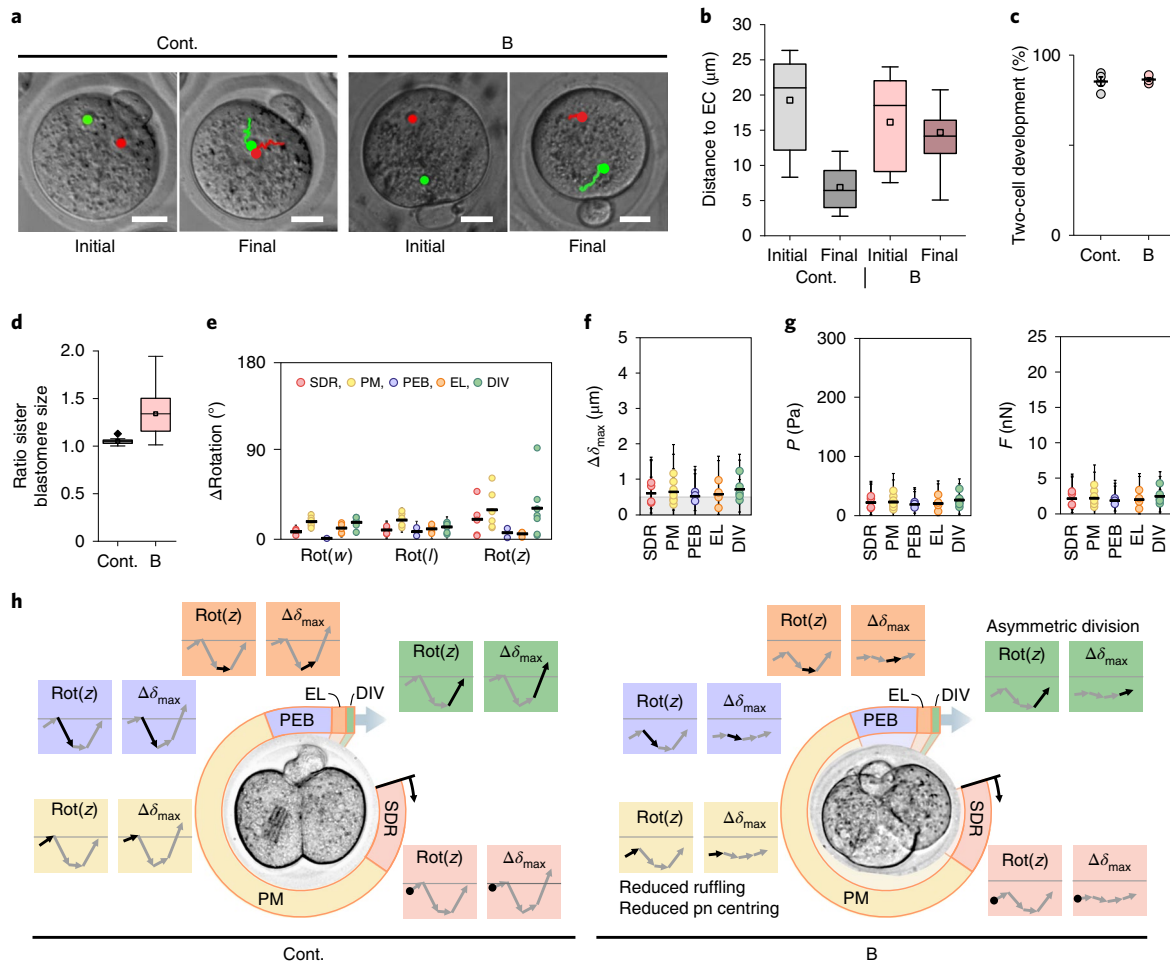


Fig. 6 | Tracking perturbation to the mechanical programme of mouse embryos. **a**, Representative time-lapse images of embryos ($n=2$ each) cultured without (control, Cont.) or with blebbistatin (B; $200 \mu\text{M}$). Images are of embryos immediately after pronuclear formation (Initial) and at PEB (Final), showing starting and final positions (large dots) and trajectories of female (green) and male (red) pronuclei. Scale bar, $20 \mu\text{m}$. **b**, Box-and-whiskers plots showing distances between pronuclei and embryo centres at initial (pronuclear formation) and final (PEB) positions ($n \geq 5$) following culture as for **a**. Whiskers, 0 to 99th percentile; box, 25th to 75th percentile; line within box, median. Values (respectively maximum, mean, minimum): Cont. (initial) 26.34, 19.25, 8.32; (final) 12.00, 6.87 and 2.78; B (initial) 24.00, 16.14, 7.55; (final) 20.74, 14.68, 5.08. Quantile calculations excluded the median. **c**, Percentage of control (Cont.) one-cell embryos ($n=77$) or one-cell embryos cultured in blebbistatin (100 or $200 \mu\text{M}$; $n=121$), cleaving to two cells after 24 h. Dot plots show percentages on four experimental days. Black horizontal lines indicate mean values \pm s.e.m. **d**, Percentages of control embryos (Cont.; $n=10$) or embryos cultured in $200 \mu\text{M}$ blebbistatin (B; $n=22$) undergoing asymmetric division. Data are box-and-whiskers plots (whiskers, 0 to 99th percentile; box, 25th to 75th percentile; line within box, median). Values (maximum, mean, minimum): Cont., 1.08, 1.05, 1.00; B, 1.94, 1.34 1.01. **e, f**, Maximum intracellular device rotations $\text{Rot}(w)$ ($n=21$), $\text{Rot}(l)$ ($n=24$) and $\text{Rot}(z)$ ($n=25$) (**e**) and $\Delta\delta_{\text{max}}$ during embryo stages (**f**) ($n=23$). Grey indicates range of lower confidence. **g**, Simulated pressure and force acting on the nanodevice necessary to obtain given values of $\Delta\delta_{\text{max}}$. Data of **e-g** are for embryos cultured in blebbistatin, with bars depicting error propagation. **h**, Models of the mechanical programme for controls (Cont.) and embryos perturbed by blebbistatin treatment (B). n refers to biologically independent samples throughout.

intracytoplasmic sperm injection (ICSI) that we examined (Fig. 5b), suggesting that the underlying mechanics are shared. These plots incorporated changes that reflected mechanical transitions that we designated (in temporal order), EL1, EL2 and DIV (Fig. 5a).

Immunofluorescence images of embryos revealed changes in microtubule organization coinciding with EL1, EL2 and DIV (Fig. 5c). EL1 microtubules shape the spindle and localize cortically with F-actin, augmenting cortical stiffness. At EL2 (just before cleavage furrow formation at the embryo centre), a tubulin meshwork³⁹ appeared in the equatorial region (Fig. 5c). Radial microtubules then increasingly emanated from spindle poles, first towards their proximal overlying equatorial cortex and subsequently (during DIV), towards polar cortical regions (Fig. 5c), when elongation practically stopped.

Overall, EL-phase embryos experienced the largest global deformation, but nanodevices counterintuitively reported the smallest rotations (Fig. 2c), indicating minimal cytoplasmic reorganization. Consistent with their decreased rotation, nanodevices detected the greatest ξ_k at EL (Fig. 2f). The fact that the embryo normally elongated even though radial microtubules were absent (Fig. 5c,d) suggests that the mechanical load generated by the elongating spindle is transmitted through the bulk cytoplasm to the axial cortex. Immunofluorescence images of actin and myosin II distribution showed an increment of myosin II from EL1 to EL2 (Fig. 5c,d), in agreement with previously suggested myosin-mediated cytoplasmic stiffening. This directly demonstrates that the cytoplasmic stiffness of mouse embryos increases during the EL phase, accompanied by an increase in myosin II activity. Such stiffening would enhance

spindle force transmission to the embryo cortex during elongation. Coarse spindle centring is facilitated by spindle elongation (given the stiffer cortex), in agreement with the GES model.

Cytoplasmic softening and the largest forces during division.

During the brief division (DIV) phase (lasting 5.5 ± 1.6 min), nanodevices near the cleavage plane underwent rotations of up to $137 \pm 2^\circ$ and deformations of $4.2 \pm 0.3 \mu\text{m}$ (Fig. 2c,d and Fig. 5e,f), corresponding to $P = 233 \pm 20$ Pa (17.7 ± 1.5 nN) (Fig. 2e). Maximal ξ_{mact} was approximately two orders higher than at any other time in the embryo (Fig. 2f). Combined with the rapidity of nanodevice bending and relaxation (Fig. 5e,f and Supplementary Video 8) this suggested a decrease in ξ_k during DIV, as detected by the devices (Fig. 2f) indicating active softening of the cytoplasm. Changes in cytoplasmic stiffness correlated with cytoplasmic myosin II dynamics (Fig. 5g). Close to DIV completion, spindle and radial microtubules underwent a collective motion similar to an umbrella folding as each of the two chromosome sets moved towards their respective cortical pole (Fig. 5h,i). The fact that chromosome sets are located close to the embryo poles, combined with the large ξ_{mact} revealed by the nanodevices, suggested that the chromosomes are localized further from the division plane, where cytoplasmic reorganization is greater; this could help guarantee chromosome segregation to respective daughter cells. Radial microtubule disassembly (Fig. 5h,i) as the DIV phase ended resembled recently described microtubule behaviour⁴⁰. Rapid cleavage plane progression, cytoplasmic reorganization and chromosome positioning away from the division plane would be facilitated by the low cytoplasmic stiffness reported by the nanodevices.

Experimental perturbation of the mechanical programme. This work predicts a programme of mechanical and force changes within embryos that we next evaluated via perturbation experiments. We reasoned that this might be achieved by the actomyosin (myosin II) motor inhibitor, blebbistatin, to reduce force generation⁴¹ and cytoplasmic stiffness⁴² within the embryo. Accordingly, embryos incubated in the presence of blebbistatin underwent a reduction in cortical ruffling and pronuclear convergence during the PM phase relative to untreated controls (Fig. 6a,b and Supplementary Video 9). In controls, pronuclei and other large cytoplasmic structures moved comparatively little, but with blebbistatin treatment they exhibited greater random movement (Supplementary Video 9), consistent with a reduction in cytoplasmic stiffness⁴². Exposure to blebbistatin did not prevent embryo division (Fig. 6c and Supplementary Fig. 17) but division was asymmetric (Fig. 6d).

Compared to unexposed controls (Fig. 2c–e), nanodevices within blebbistatin-treated embryos exhibited a marked reduction in rotation (related to cytoplasmic reorganization) and mechanical loads throughout much of the one-cell stage (Fig. 6e–g), further evidencing a functional role for the actomyosin complex in force generation. In addition, the reduced forces and increased random pronuclear movement in blebbistatin-treated embryos provided evidence for a reduction in effective stiffness caused by myosin inhibition⁴².

Although blebbistatin-treated PM-phase embryos experienced a twofold cytoplasmic mechanical load reduction (Figs. 2e and 6g), pronuclear centring was reduced by roughly tenfold, suggesting that cytoplasmic forces alone are not sufficient to account for pronuclear centring (Fig. 6b). The reduction in cytoplasmic stiffness caused by blebbistatin would also reduce spindle force transmission to the cortex, leading to aberrant spindle centring followed by asymmetric division (Fig. 6d).

Discussion

This work adopts a top-down approach that identifies a programme of intracellular force and mechanical property changes during mouse one-cell embryo development. Intracellular nanodevices responded stereotypically throughout, revealing a programme of

cytoplasmic force and stiffness changes that map to developmental progression. Nanodevice deflections during the SDR phase revealed major mechanical activity that coincided with dynamic paternal chromatin remodelling²⁹. This is possibly the first direct force measurement associated with any intracellular genome reprogramming, with relevance to chromatin remodelling^{43,44}. The GES model considers the effects on cytoplasmic effective mechanical properties due to boundary conditions. Although it is descriptive in nature, given the molecular nature of some of the force generators and the unknown role played by cytoplasmic heterogeneity, it explains why pronuclear displacement is larger in the direction of centre of the embryo during the PM phase, predicts the contribution of pronuclear growth to centring and is compatible with force gradient models. Spindle alignment throughout the PEB phase is facilitated by reducing cytoplasmic mechanical activity and could act as a mechanism to avoid chromosome mis-sorting during cell division.

During the EL phase, nanodevices reported high cytoplasmic resistance to reorganization that counterintuitively occurred in the absence of radial microtubules. Such cytoplasmic stiffening would enhance spindle centring and the transmission to the cortex of mechanical loads exerted by spindle elongation. Acute softening of the cytoplasm would be required for rapid cleavage plane progression and extensive cytoplasmic reorganization⁴⁰ during cell scission. Cytoplasmic forces larger than 10 nN were detected that may indeed be necessary during completion of the first cell cycle in mouse embryonic development, and it is notable that our devices measure average forces driving cytoplasmic reorganization rather than intracellular point forces. For example, the devices tracked large average reductions in cytoplasmic mechanical loads and cytoplasmic redistribution after blebbistatin perturbation (Fig. 6h), in agreement with consequential reduction in pronuclear centring and increased asymmetric division.

Collectively, these findings are consistent with fundamental roles for intracellular forces and cytoplasmic mechanical dynamics in early mammalian development (Fig. 5a,b). We anticipate that the work will open a window onto intracellular physics and provide complementary information to existing techniques for mechanobiology.

Online content

Any methods, additional references, Nature Research reporting summaries, source data, extended data, supplementary information, acknowledgements, peer review information; details of author contributions and competing interests; and statements of data and code availability are available at <https://doi.org/10.1038/s41563-020-0685-9>.

Received: 17 April 2018; Accepted: 16 April 2020;

Published online: 25 May 2020

References

- Kollmannsberger, P. & Fabry, B. Linear and nonlinear rheology of living cells. *Ann. Rev. Mat. Res.* **41**, 75–97 (2011).
- Guo, M. et al. Probing the stochastic, motor-driven properties of the cytoplasm using force spectrum microscopy. *Cell* **158**, 822–832 (2014).
- Davidson, L., von Dassow, M. & Zhou, J. Multi-scale mechanics from molecules to morphogenesis. *Int. J. Biochem. Cell Biol.* **41**, 2147–2162 (2009).
- Savin, T. et al. On the growth and form of the gut. *Nature* **476**, 57–62 (2011).
- Farge, E. Mechanical induction of Twist in the *Drosophila* foregut/stomodaeal primordium. *Curr. Biol.* **13**, 1365–1377 (2003).
- Kahn, J. et al. Muscle contraction is necessary to maintain joint progenitor cell fate. *Dev. Cell* **16**, 734–743 (2009).
- Mammoto, A., Mammoto, T. & Ingber, D. E. Mechanosensitive mechanisms in transcriptional regulation. *J. Cell Sci.* **125**, 3061–3073 (2012).
- Chen, D. T. N., Wen, Q., Janmey, P. A., Crocker, J. C. & Yodh, A. G. Rheology of soft materials. *Ann. Rev. Condens. Matter Phys.* **1**, 301–322 (2010).
- Moeendarbary, E. et al. The cytoplasm of living cells behaves as a poroelastic material. *Nat. Mater.* **12**, 253–261 (2013).
- Roca-Cusachs, P., Conte, V. & Trepast, X. Quantifying forces in cell biology. *Nat. Cell Biol.* **19**, 742–751 (2017).

11. Bao, G. & Suresh, S. Cell and molecular mechanics of biological materials. *Nat. Mater.* **2**, 715–725 (2003).
12. Lim, C. T., Zhou, E. H. & Quek, S. T. Mechanical models for living cells—a review. *J. Biomech.* **39**, 195–216 (2006).
13. Trepap, X. et al. Universal physical responses to stretch in the living cell. *Nature* **447**, 592–595 (2007).
14. Polacheck, W. J. & Chen, C. S. Measuring cell-generated forces: a guide to the available tools. *Nat. Methods* **13**, 415–423 (2016).
15. Trepap, X., Lenormand, G. & Fredberg, J. J. Universality in cell mechanics. *Soft Mat.* **4**, 1750–1759 (2008).
16. Keren, K., Yam, P. T., Kinkhabwala, A., Mogilner, A. & Theriot, J. A. Intracellular fluid flow in rapidly moving cells. *Nat. Cell Biol.* **11**, 1219–1224 (2009).
17. Zimmerman, J. F. et al. Free-standing kinked silicon nanowires for probing inter- and intracellular force dynamics. *Nano Lett.* **15**, 5492–5498 (2015).
18. Hendricks, A. G. & Goldman, Y. E. Measuring molecular forces using calibrated optical tweezers in living cells. *Methods Mol. Biol.* **1486**, 537–552 (2017).
19. Gómez-Martínez, R. et al. Silicon chips detect intracellular pressure changes in living cells. *Nat. Nanotechnol.* **8**, 517–521 (2013).
20. Torras, N. et al. Suspended planar-array chips for molecular multiplexing at the microscale. *Adv. Mater.* **28**, 1449–1454 (2016).
21. Discher, D. E., Mooney, D. J. & Zandstra, P. W. Growth factors, matrices, and forces combine and control stem cells. *Science* **26**, 1673–1677 (2009).
22. Lutolf, M. P., Gilbert, P. M. & Blau, H. M. Designing materials to direct stem-cell fate. *Nature* **462**, 433–441 (2009).
23. Maitre, J. L., Niwayama, R., Turlier, H., Nédélec, F. & Hiiragi, T. Pulsatile cell-autonomous contractility drives compaction in the mouse embryo. *Nat. Cell Biol.* **17**, 849–855 (2015).
24. Lehtonen, E. Changes in cell dimensions and intercellular contacts during cleavage-stage cell cycles in mouse embryonic cells. *J. Embryol. Exp. Morphol.* **58**, 231–249 (1980).
25. Tzur, A., Kafri, R., LeBleu, V. S., Lahav, G. & Kirschner, M. W. Cell growth and size homeostasis in proliferating animal cells. *Science* **325**, 167–171 (2009).
26. Zhou, L. & Dean, J. Reprogramming the genome to totipotency in mouse embryos. *Trends Cell Biol.* **25**, 82–91 (2015).
27. Campàs, O. et al. Quantifying cell-generated mechanical forces within living embryonic tissues. *Nat. Methods* **11**, 183–189 (2014).
28. Hyman, A. A., Weber, C. A. & Jülicher, F. Liquid-liquid phase separation in biology. *Ann. Rev. Cell Dev. Biol.* **30**, 39–58 (2014).
29. Yoshida, N., Brahmajosyula, M., Shoji, S., Amanai, M. & Perry, A. C. F. Epigenetic discrimination by mouse metaphase II oocytes mediates asymmetric chromatin remodeling independently of meiotic exit. *Dev. Biol.* **301**, 464–477 (2007).
30. Suzuki, T. et al. Mice produced by mitotic reprogramming of sperm injected into haploid parthenogenotes. *Nat. Commun.* **7**, 12676 (2016).
31. Rai, A. K., Rai, A., Ramaiya, A. J., Jha, R. & Mallik, R. Molecular adaptations allow dynein to generate large collective forces inside cells. *Cell* **152**, 172–182 (2013).
32. Payne, C., Rawe, V., Ramalho-Santos, J., Simerly, C. & Schatten, G. Preferentially localized dynein and perinuclear dynactin associate with nuclear pore complex proteins to mediate genomic union during mammalian fertilization. *J. Cell Sci.* **116**, 4727–4738 (2003).
33. Chaigne, A. et al. F-actin mechanics control spindle centring in the mouse zygote. *Nat. Commun.* **7**, 10253 (2016).
34. Rowat, A. C., Lammerding, J. & Ipsen, J. H. Mechanical properties of the cell nucleus and the effect of emerin deficiency. *Biophys. J.* **91**, 4649–4664 (2006).
35. Hose, Basarab G. et al. Reversible disassembly of the actin cytoskeleton improves the survival rate and developmental competence of cryopreserved mouse oocytes. *PLoS ONE* **3**, e2787 (2008).
36. Sutovsky, P., Simerly, C., Hewitson, L. & Schatten, G. Assembly of nuclear pore complexes and annulate lamellae promotes normal pronuclear development in fertilized mammalian oocytes. *J. Cell Sci.* **111**, 2841–2854 (1998).
37. Chew, T. G., Lorthongpanich, C., Ang, W. X., Knowles, B. B. & Solter, D. Symmetric cell division of the mouse zygote requires an actin network. *Cytoskeleton* **69**, 1040–1046 (2012).
38. Yu, X. J. et al. The subcortical maternal complex controls symmetric division of mouse zygotes by regulating F-actin dynamics. *Nat. Commun.* **5**, 4887 (2014).
39. Schatten, G., Simerly, C. & Schatten, H. Microtubule configurations during fertilization, mitosis, and early development in the mouse and the requirement for egg microtubule-mediated motility during mammalian fertilization. *Proc. Natl Acad. Sci. USA* **82**, 4152–4156 (1985).
40. Zenker, J. et al. A microtubule-organizing center directing intracellular transport in the early mouse embryo. *Science* **357**, 925–928 (2017).
41. Ajduk, A. et al. Rhythmic actomyosin-driven contractions induced by sperm entry predict mammalian embryo viability. *Nat. Commun.* **2**, 417 (2011).
42. Schäfer, A. Influence of myosin II activity on stiffness of fibroblast cells. *Acta Biomater.* **1**, 273–280 (2005).
43. Strom, A. R. et al. Phase separation drives heterochromatin domain formation. *Nature* **547**, 241–245 (2017).
44. Larson, A. G. et al. Liquid droplet formation by HP1 α suggests a role for phase separation in heterochromatin. *Nature* **547**, 236–240 (2017).

Publisher's note Springer Nature remains neutral with regard to jurisdictional claims in published maps and institutional affiliations.

© The Author(s), under exclusive licence to Springer Nature Limited 2020

Methods

Chip fabrication. Substrates had a diameter of 100 mm and were 500- μm -thick P-type <100> silicon wafers (Si-Mat, Silicon Materials). A 100-nm-thick SiO_2 TEOS tetraethylorthosilicate [$[\text{Si}(\text{OC}_2\text{H}_5)_4]$] layer was deposited by plasma-enhanced chemical vapour deposition. A polysilicon layer 25 to 500 nm thick was deposited by chemical vapour deposition (630 °C, 120 mTorr) and a 1.2- μm -thick positive photoresist then spun onto the wafers (ma-P 6512 Micro Resist Technology). Exposure to ultraviolet light (Stepper NSR1505-G7E; Nikon) was performed through the reticule. The resist was developed, baked (30 min, 200 °C) and the polysilicon layer etched using SF_6 and $\text{c-C}_4\text{F}_8$ (ALCATEL 601E; Alcatel) before the photoresist was stripped (TEPLA 300-E, Technics Plasma). Finally, chips were released by SiO_2 sacrificial etching in 49% (v/v) hydrogen fluoride vapour for 40 min and resuspended in 96% ethanol with short ultrasonic pulses. Due to their fragility, centrifugation was impracticable and devices were collected by settling in Eppendorf tubes. Microelectronic techniques for device production allow enormous precision both in the thickness of their layers and in lateral dimensions (Supplementary Fig. 2); polysilicon has historically played an important role in the microelectronics industry and the technology is accordingly highly evolved. Consideration to the stress gradient and the quality of the surface of the 25-nm-thick polysilicon layer requires careful optimization of the deposition process that will depend on the deposition equipment used. Release of the devices cannot be achieved by ultrasound due to their fragility. Rather, we liberate devices from the substrate by immersion in ethanol and careful rinsing with recirculated ethanol using a micropipette. The released chips are washed thoroughly in ethanol to remove residual hydrogen fluoride, which otherwise can affect embryo viability. Centrifugation of the chips was avoided, and devices allowed to settle out of suspension or collected by filtering. After the final collection, devices were gently resuspended in sterile, pure water. Manipulation was performed manually with care to avoid device fracture and sticking to each other. Fabrication of the chips should be readily achievable in adequately resourced MEMS laboratories.

Fabrication of optical test structures. Substrates were provided by 800- μm -thick Fused Silica wafers (Si-Mat). An aluminium layer (100 nm thick) was deposited by sputtering (Leybold Z550) on top of the wafer. The wafer was then diced to form $1 \times 1 \text{ cm}^2$ chips. A CSAR62 (ALLRESIT) resist was spun onto the chips and an electron beam lithography process (RAITH 150 (two)) permitted the definition of structures with nanometre precision. The resist was developed by ARS600-546 (ALLRESIT). A dry etching process was subsequently used to pattern the aluminium layer using SENTEC equipment, the resist removed by PVA TEPLA 300SA and the resulting structures calibrated in a scanning electron microscope (LEO 1530) at a resolution of <20 nm.

Animal care. Experiments involving animals were performed in accordance with local and national statutes including the University of Bath Animal Welfare Ethical Review Body, protecting animals in experimental research and complied with the UK Animals (Scientific Procedures) Act, 1986 and its embodiments. The study did not involve wild animals or animals collected in the field.

Collection, culture and parthenogenetic activation of mouse metaphase II oocytes. Oviductal metaphase II (mII) oocyte complexes were typically collected in M2 medium (EMD Millipore)⁴⁵ from 8–12-week-old Institute of Cancer Research females (bred in-house) or B6D2F₁ females (C57BL/6 females crossed with DBA/2 males in-house) 12–15 h after standard superovulation by serial injection of equine and human chorionic gonadotropin, as previously described^{46,47}. Cumulus cells were dispersed from cumulus-oophorous complexes by hyaluronidase treatment and after multiple washing in M2 medium, denuded oocytes incubated in potassium simplex optimized medium (KSOM; Millipore) under mineral oil in humidified 5% CO_2 (v/v in air) at 37 °C, until required. Embryo culture was typically also in KSOM (Millipore) under mineral oil in humidified 5% CO_2 (v/v in air) at 37 °C. Parthenogenetic activation of mII oocytes was by exposure to calcium-free culture medium containing 10 mM SrCl_2 initiated 16–17.5 h post human chorionic gonadotropin, essentially as described³⁰.

Human embryo videos. No human embryos were produced for the purpose of this study. Morphometric analysis of human embryos was performed using pre-existing time-lapse videos that had been subject to Institutional Review Board approval (no. NCT02852356; ClinicalTrials.gov) and consent from patients (at least 18 years old) undergoing assisted reproduction treatment at Ovation Fertility, USA. Patients had undergone ovarian stimulation according to guidelines of the treating clinic, including agonist luteal phase, agonist micro dose flare and antagonist suppression. Oocytes had been fertilized by ICSI on the day of oocyte retrieval, and immediately after assessment, apparently healthy bi-pronuclear one-cell embryos placed into a multiwell Culture Coin in a MIRI TL incubator (ESCO) containing 6% (v/v) CO_2 and a reduced level of oxygen (6% (v/v)). The microwell format of the dish housed individual embryos separately, one per media droplet. Embryos were imaged at 5-min intervals over seven focal planes. To optimize continuous and uninterrupted imaging, no media changes were performed. Videos were coded to ensure total patient anonymity before analysis.

Mouse sperm preparation and micromanipulation. Cauda epididymal sperm from 8–12-week-old B6D2F₁ males were triturated at ambient temperature (25 °C) for 45 s in nuclear isolation medium (125 mM KCl, 2.6 mM NaCl, 7.8 mM Na_2HPO_4 , 1.4 mM KH_2PO_4 , 3.0 mM EDTA; pH 7.0) containing 1.0% (w/v) 3-((3-cholamidopropyl)dimethylammonio)-1-propanesulfonate (CHAPS)^{30,48,49}. They were then washed twice at 25 °C in nucleus isolation medium (NIM) and pelleted (1,890g); head-tail detachment was enhanced by trituration during pellet resuspension. Finally, sperm were resuspended in ice-cold NIM (~0.5 ml per epididymis) and kept at 4 °C or on ice for up to 3 h until required. Approximately 50 μl of each suspension was mixed by trituration using a 'cut-off' yellow Gilson tip with 20 μl of polyvinylpyrrolidone (PVP, average $M_n \approx 360,000$; Sigma-Aldrich) solution (15% (w/v)) and sperm injected (ICSI) into oocytes in a droplet of M2 within ~60 min of sperm-PVP mixing⁴⁷. After a brief recovery period (~5 min), injected oocytes were transferred to KSOM under mineral oil equilibrated in humidified 5% CO_2 (v/v in air) at 37 °C.

Nanodevice injection. Microinjection of nanodevices with or without a sperm head was performed in M2 medium under mineral oil using a piezo micromanipulator following a previously described protocol⁴⁷. Immediately before microinjection, ~50 μl of freshly prepared sperm suspension was mixed with 20 μl of PVP (average $M_n \approx 360,000$; Sigma-Aldrich) solution (4% (w/v)) in NIM. Injection was within ~60 min of PVP mixing. Nanodevices were similarly prepared by mixing with 4% (w/v) PVP just before injection. Where appropriate, a single sperm head was drawn into the needle followed by a single nanodevice and injected together into an mII oocyte. Some injections were of one nanodevice or small ($3 \times 3 \mu\text{m}^2$) nanosquares. Injection needles were fabricated on a Flaming–Brown Model P-97 micropipette puller (Sutter Instrument Co.) using settings standard for ICSI pipettes: $P = 500$, $\text{heat} = 820$, $\text{pull} = 100$, $\text{vel} = 130$, $\text{time} = 100$. Pipettes were pulled to give needles of ~6–20 μm internal diameter, in each case slightly larger than the respective object they would be employed to inject. Piezo (Prime Tech) settings were: intensity (3–6), speed (4–7) depending on the needle for zona penetration; intensity (1, sometimes 2), speed (1) for oocyte plasma membrane breakage. The DNA-conjugated latex microbeads of Supplementary Fig. 11 were prepared and injected into mII oocytes as previously reported³⁰ and analysed by immunocytochemistry ~4 h after injection.

Oocytes in a given batch were injected within 15 min of each other and after a brief recovery period (~5 min), transferred to KSOM medium under mineral oil equilibrated in humidified 5% CO_2 (v/v in air) at 37 °C and cultured until required.

Because injected nanodevices are free to move in the cytoplasm, it is not possible to dictate their localization apart from their approximate placement near the beginning of development in the SDR phase, soon after injection. Thus, the measured data for each phase represent different device positions inside a given embryo, reporting the overall cytoplasmic mechanics. The coinjection of multiple devices into a single oocyte might mitigate against this, but is technically extremely challenging and would result in the potentially toxic introduction of excessive volumes of injection medium.

Some analyses were of embryos incubated in the presence of the myosin II inhibitor, blebbistatin. To this end, embryos were produced by sperm injection (ICSI) and transferred within ~1 h in the dark to KSOM medium supplemented with 200 μM of blebbistatin (Sigma, B0560) under mineral oil and incubation continued.

Utr-mCherry construct generation and complementary RNA injection.

Utr was expressed as an mCherry fluorescent fusion encoded by recombinant cRNA. To this end, a *NheI-XhoI* fragment from PCR II Utr⁵⁰ was cloned into the backbone vector, pCI-Neo-mCherry⁴⁶, to generate pCI-Neo-Utr-mCherry. Linearized plasmid template DNA prepared using the Endo Free Plasmid Maxi Kit (Qiagen) was used to prime synthesis in vitro of 5'-capped and polyadenylated cRNA⁵¹ by a T7 mScript Standard messenger RNA Production System (CellsScript) according to the recommendations of the manufacturer. cRNAs were dissolved in nuclease-free water, quantified on a NanoPhotometer (Implen) and stored in aliquots at –80 °C until required. cRNA solutions were diluted with sterile water and injected into mII oocytes in M2 medium at a concentration of 1 mg ml^{-1} within 1 h of thawing, via a piezo-actuated micropipette. After injection of *Utr-mCherry* cRNA, oocytes were returned to KSOM medium under mineral oil equilibrated in humidified 5% CO_2 (v/v in air) at 37 °C and injected ~3 h later with sperm and with or without a nanodevice.

Immunocytochemistry. Oocytes and embryos were fixed in 4% (w/v) paraformaldehyde and either processed immediately or stored at 4 °C until required. Fixed cells were permeabilized by incubation in PBS supplemented with 0.5% (v/v) triton X-100 and 0.1% (w/v) BSA for 30 min at 37 °C, followed by blocking in PBS supplemented with 3% (v/v) normal goat serum and 0.1% (w/v) BSA for 30 min at room temperature. Primary antibody labelling was by incubating samples overnight at 4 °C with the primary antibody followed by a 1 h incubation at 37 °C with the appropriate secondary antibody (1:250 (v/v); Life Technologies) conjugated to Alexa 488 and/or Alexa 594. Primary antibodies were: anti-alpha tubulin antibody (Merck, catalogue no. T9026-100L, clone DM1A; 1:2,000 (v/v) dilution); anti-Myosin IIb antibody (Cell Signaling, catalogue no. 3404, 1/200 [v/v]

dilution). Phalloidin (Thermo Fisher Scientific, catalogue no. A12379) was used to stain F-actin at a dilution of $1:2 \times 10^5$ (v/v). DNA was stained by incubating samples at 37 °C for 20 min in propidium iodide (1:200 (v/v); Sigma-Aldrich).

Ratiometric quantitative PCR. Ratiometric transcript quantification of one-cell embryos generated with or without nanodevice injection (Supplementary Fig. 10) was essentially as described previously³⁰. Real-time quantitative PCR was in an ABI 7500 Real-Time PCR System (Applied Biosystems, CA) in reactions (20 μ l in total) containing 1–2 μ l of the template complementary DNA, forward and reverse primers (100 nM each) and 12.5 μ l of Power SYBR (ABI). Each experiment was performed on at least two experimental days and included technical duplicates of each sample. Primer sets (Hokkaido System Science or Eurofins MWG Operon) were non-dimerizing under the conditions employed and their sequences were (each shown 5' \rightarrow 3'): *H1foo* F, ATGGAGGCCAGAAGGTCAAAC; *H1foo* R, TCTCAGCCCCCTGAACAAC; *Kpna2* F, GTGATGGTTCAGCTTTCCGAG; *Kpna2* R, GTGCAGGGTTCTTGTTCGAC; *Ik* F, GATGTTGACAAAGGACC TGGA; *Ik* R, ATCGTGGCTGGATAGCATTC; *Kanadaptin* F, AGCATGAAGAAC GAGTGGAGG; *Kanadaptin* R, GGTGCTGCATGGCTTTAGTC; *Ube2a* F, CCC GTTTGAGGATGGAACAT; *Ube2a* R, TGGACTCCAACGGTTCGAAG; *Slc4a1apv1* F, GTCATGTGAGGACCCTTCAG and *Slc4a1apv2* R, ACTTTGACCT TCAGGTGGGA. Reverse transcriptase-minus controls were processed in parallel and reactions lacking input cDNA served to verify absence of contaminants.

Image collection and analysis. This section describes microscope and software parameters used in time-lapse video image acquisition. Images of live oocytes or embryos following crRNA injection were captured on an Olympus IX71 equipped with an Andor Zyla VSC-00497-5.5 sCMOS camera with XY calibration corresponding to a pixel size of 6.5 μ m and OptoLED illumination system (Cairn Research) and processed using Metamorph software (Molecular Devices). Some images represent video captures (vidcaps) from videos taken on an IX71 framework (Olympus) using a $\times 40$ objective, 0.6 numerical aperture (NA) with $\times 1.6$ zoom. Other images were generated using a $\times 60$ objective (DO/LUCPLFLN60X PH/ NA 0.7, Universal C-plan Fluorite). Excitation at 587 nm in combination with an ET-mCherry filter system was used for mCherry fluorescence detection. Confocal images were obtained with an Eclipse E600 (Nikon) microscope equipped with a Radiance 2100 laser scanning system (BioRad and LSM Technical Service). Time-lapse videomicroscopy captured images at 300 ms to 5.0 min intervals with or without fluorescence illumination of alternate frames with 1–10 z-slices, each 2 μ m thick. Embryo development was slower in some time-lapse fluorescence videos. Time-lapse video construction and analysis were performed with Metamorph v.7.8.12.0 or using the selection tool of ImageJ (<http://rsbweb.nih.gov/ij/>). Outputs are shown relative to corresponding similarly determined controls as described. Three to ten (but typically seven) images were acquired per z stack at each time-point, each image corresponding to a step size of 2 μ m. Error bars in Figs. 2d and 6f are calculated by the two-pixel error in P1, P2 and P3 localization (Supplementary Fig. 13) and the propagation of this error through the calculation of δ and $\Delta\delta_{\max}$.

For analysis of particle density (independently of size) in strain 129/SvJ one-cell embryos (Supplementary Fig. 16), we designated a subcortical zone extending around the embryo between the plasma membrane and 10 μ m beneath it (outer), and separated this in our analysis from the remaining embryo interior (inner). Embryo images were converted to binary and analysed with edge finding and plot profiling tools (ImageJ). Peaks in plot profiling with values more than ten (grey values) were counted in standardized sampling areas across embryos and plotted as average numbers of peaks, with each peak corresponding to a particulate cytoplasmic discontinuity for 'inner' and 'outer' areas.

Nanodevice displacement and bending and the mechanobiology of mouse embryos. The direct, simultaneous monitoring of intracellular force dynamics and of changes to the resistance to cytoplasmic reorganization during different phases of mouse one-cell embryo development after fertilization provide important new information about the role of cell mechanics at the onset of embryogenesis (Supplementary Fig. 1). Nanodevice rotation and translation (the displacement vector, **d**) describes cytoplasmic reorganization and is a consequence of changes in intracellular mechanical loads (the force vector, **F**). The level of intracellular forces can be determined by measuring the bending of the devices. How forces, **F**, affect cytoplasmic reorganization, **d**, depends in part on the mechanical properties of the cytoplasm. This means that changes in the mechanical properties of the cytoplasm (Fig. 2f) can be inferred by determining the level of mechanical loads (forces or pressures) (Fig. 2e) and measuring nanodevice rotations (Fig. 2c) or translations

inside the embryo. Thus, intracellular forces and cytoplasmic resistance to deformation contribute to the behaviour of cytoplasmic reorganization and we accordingly define an ad hoc theoretical parameter, $\xi_k = F_{\max}/\text{Rot}_{\max}^k$, providing information about the resistance to cytoplasmic reorganization that in turn gives information about intracellular property changes (Fig. 2f).

Statistical analysis. All experiments were performed on at least 2 d to give biological replicates. Data points (*n*) refer to independent sample (typically embryo) numbers unless stated otherwise, and data analysis performed without blinding. Statistical differences between pairs of data sets were analysed by chi-squared or two-tailed unpaired *t*-tests. Values of $p < 0.05$ were considered statistically significant.

Reporting Summary. Further information on research design is available in the Nature Research Reporting Summary linked to this article.

Data availability

Supporting data are available in the Source Data files and from the corresponding authors upon reasonable request.

References

- Quinn, P., Barros, C. & Whittingham, D. G. Preservation of hamster oocytes to assay the fertilizing capacity of human spermatozoa. *J. Reprod. Fertil.* **66**, 161–168 (1982).
- Shoji, S. et al. Mammalian Emi2 mediates cytostatic arrest and transduces the signal for meiotic exit via Cdc20. *EMBO J.* **25**, 834–845 (2006).
- Yoshida, N. & Perry, A. C. F. Piezo-actuated mouse intracytoplasmic sperm injection (ICSI). *Nat. Protoc.* **2**, 296–304 (2007).
- Perry, A. C. F., Wakayama, T., Cooke, I. M. & Yanagimachi, R. Mammalian oocyte activation by the synergistic action of discrete sperm head components: induction of calcium transients and involvement of proteolysis. *Dev. Biol.* **217**, 386–393 (2000).
- Suzuki, T., Asami, M. & Perry, A. C. F. Asymmetric parental genome engineering by Cas9 during mouse meiotic exit. *Sci. Rep.* **4**, 7621 (2014).
- Burkel, B. M., von Dassow, G. & Bement, W. M. Versatile fluorescent probes for actin filaments based on the actin-binding domain of utrophin. *Cell Motil. Cytoskeleton* **64**, 822–832 (2007).
- Suzuki, T. et al. Mouse Emi2 as a distinctive regulatory hub in second meiotic metaphase. *Development* **137**, 3281–3291 (2010).

Acknowledgements

We are grateful to B. Nichols, J. Campos, T. Suárez and C. Tickle for their constructive comments during manuscript preparation and thank Animal Facility support staff for ensuring the welfare of animals used in this work. We are deeply indebted to the late Dino Sharma for help with image collection. We acknowledge support to A.C.F.P. from the Medical Research Council, UK (grant nos. G1000839, MR/N000080/1 and MR/N020294/1) and the Biology and Biological Science Research Council, UK (grant no. BB/P009506/1) and to J.A.P. from the Spanish Government, grant nos. TEC2014-51940-C2 and TEC2017-85059-C3 with Feder funding. We also thank the clean room staff of IMB-CNM for assistance with chip fabrication.

Author contributions

A.C.F.P. and J.A.P. conceived core experiments. M.D., R.G.-M. and J.A.P. performed nanodevice fabrication, T.S. and M.A. performed microinjection and embryo production and M.A. and M.D.V. undertook image collection. Data analysis and modelling were by N.T., M.A., M.I.A., R.C. and J.A.P. A.C.F.P. and J.A.P. wrote most of the manuscript with contributions from the other authors.

Competing interests

The authors declare no competing interests.

Additional information

Supplementary information is available for this paper at <https://doi.org/10.1038/s41563-020-0685-9>.

Correspondence and requests for materials should be addressed to J.A.P. or A.C.F.P.

Reprints and permissions information is available at www.nature.com/reprints.